Involvement of Aryl hydrocarbon receptor in myelination and in human nerve sheath tumorigenesis

Ghjuvan'Ghjacumu Shackleford[a,1], Nirmal Kumar Sampathkumar[a,1], Mehdi Hichor[a], Laure Weill[a], Delphine Meffre[a], Ludmila Juricek[a], Ingrid Laurendeau[b], Aline Chevallier[a], Nicolas Ortonne[c], Frédérique Larousserie[d], Marc Herbin[e], Ivan Bièche[b], Xavier Coumoul[a], Mathieu Beraneck[f], Etienne-Emile Baulieu[g,2], Frédéric Charbonnier[a], Eric Pasmant[b], and Charbel Massaad[a,2]

[a]University Paris Descartes, INSERM UMR 1124, Faculty of Basic and Biomedical Sciences, 75270 Paris Cedex 6, France; [b]EA7331, Université Paris Descartes, Faculté de Pharmacie de Paris, 75270 Paris Cedex 6, France; [c]Department of Pathology, Henri Mondor Hospital, 94010 Créteil, France; [d]Department of Pathology, Cochin Hospital, 75014 Paris, France; [e]CNRS UMR 7179, Département Ecologie et Gestion de la Biodiversité, Muséum National d'Histoire Naturelle, 75231 Paris Cedex 5, France; [f]University Paris Descartes, CNRS UMR 8119, Faculty of Basic and Biomedical Sciences, 75270 Paris Cedex 6, France; and [g]Paris-Saclay University, INSERM UMR-1195, 94276 Le Kremlin-Bicêtre Cedex, France

Contributed by Etienne-Emile Baulieu, December 18, 2017 (sent for review September 18, 2017; reviewed by Ruth M. Stassart and Carles Vilarino-Guell)

Aryl hydrocarbon receptor (AHR) is a ligand-activated transcription factor involved in xenobiotic metabolism. Plexiform neurofibromas (PNFs) can transform into malignant peripheral nerve sheath tumors (MPNSTs) that are resistant to existing therapies. These tumors are primarily composed of Schwann cells. In addition to neurofibromatosis type 1 (*NF1*) gene inactivation, further genetic lesions are required for malignant transformation. We have quantified the mRNA expression levels of AHR and its associated genes in 38 human samples. We report that AHR and the biosynthetic enzymes of its endogenous ligand are overexpressed in human biopsies of PNFs and MPNSTs. We also detect a strong nuclear AHR staining in MPNSTs. The inhibition of AHR by siRNA or antagonists, CH-223191 and trimethoxyflavone, induces apoptosis in human MPNST cells. Since AHR dysregulation is observed in these tumors, we investigate AHR involvement in Schwann cell physiology. Hence, we studied the role of AHR in myelin structure and myelin gene regulation in *Ahr*$^{-/-}$ mice during myelin development. AHR ablation leads to locomotion defects and provokes thinner myelin sheaths around the axons. We observe a dysregulation of myelin gene expression and myelin developmental markers in *Ahr*$^{-/-}$ mice. Interestingly, AHR does not directly bind to myelin gene promoters. The inhibition of AHR in vitro and in vivo increased β-catenin levels and stimulated the binding of β-catenin on myelin gene promoters. Taken together, our findings reveal an endogenous role of AHR in peripheral myelination and in peripheral nerve sheath tumors. Finally, we suggest a potential therapeutic approach by targeting AHR in nerve tumors.

AHR | myelin | nerve | MPNST | neurofibroma

Neurofibromatosis type 1 (NF1, MIM162200) is an autosomal dominant neurocutaneous tumor predisposition syndrome caused by a germ-line heterozygous mutation in the *NF1* gene (1). The most common NF1-associated tumors are benign peripheral nerve sheath tumors called neurofibromas, which may be dermal or plexiform (2). Dermal neurofibromas are typically small and grow as discrete lesions in the dermis, whereas plexiform neurofibromas (PNFs) can develop internally along the plexus of major peripheral nerves and become quite large. PNFs can undergo transformation to malignant peripheral nerve sheath tumors (MPNSTs) in about 10% of NF1 patients (3). MPNSTs are resistant to conventional therapies, and their deep-seated position and locally invasive growth hinder complete surgical resection with a high degree of relapse, rendering new treatments highly indispensable. Peripheral nerve Schwann cells (SCs) are the primary pathogenic cells in neurofibromas and MPNSTs, as biallelic mutation or loss of the *NF1* gene occurs uniquely in tumor SCs (4). *NF1* encodes the RAS-GAP (Rat sarcoma GTPase activating protein) neurofibromin, and RAS signaling is elevated in neurofibroma SCs (5). Neurofibromas may develop from SCs or Schwann cell progenitors (SCPs) due to the inactivation of *Nf1* at the SCP stage or in adult mice (6, 7).

SCs carry out the myelination of axons in the nerve (8). Myelin is essential for rapid action potential propagation along the axons (9). Peripheral myelin gene expression [Myelin Protein Zero (P0) and Peripheral Myelin Protein-22 (PMP22)] is tightly regulated in SCs (10). KROX20 (11) and the Wnt/β-catenin signaling pathway (12) are known positive regulators of myelin gene expression, whereas SOX2 (13) and LXR (14) exert a negative effect.

Little is known of the additional cooperating genetic events potentially required for full PNFs' malignant transformation. Previous research from our laboratory and others have shown an activation of the Wnt signaling pathway during malignant transformation of PNFs to MPNSTs (15, 16). Indeed, the Wnt pathway is a common pathway acting on myelin development as well as malignant transformation. There is growing evidence that overactivation of the AHR (aryl hydrocarbon receptor) signaling pathway can alter Wnt/β-catenin signaling in development, different human cancers, and disease (17–19).

AHR is a ligand-activated transcription factor that is best known for mediating the toxicity and tumor-promoting properties of the carcinogen 2,3,7,8-tetrachlorodibenzo-p-dioxin (TCDD), commonly referred to as dioxin. The activation of AHR provokes its heterodimerization with AHR Nuclear Translocator (ARNT).

Significance

Aryl hydrocarbon receptor (AHR) is well known to mediate xenobiotic metabolism in vertebrates. Growing evidence reveals that AHR seems to have endogenous roles in the development and functioning of different organs. In our current study, we describe a role of AHR in peripheral myelination and in nerve sheath tumors. We show that the AHR pathway is dysregulated in human biopsies of nerve tumors. The blockade of AHR provokes cell death in nerve tumors, suggesting a therapeutic avenue in the treatment of this invasive cancer. Furthermore, the inhibition of *Ahr* in mice provokes locomotor defects and alteration of myelin structure. This work unravels an endogenous role of *Ahr* in peripheral myelination and a potential treatment of nerve tumours.

Author contributions: M.B., E.-E.B., F.C., E.P., and C.M. designed research; G.S., N.K.S., M.H., L.W., D.M., L.J., I.L., A.C., M.H., I.B., M.B., and C.M. performed research; N.O., F.L., and X.C. contributed new reagents/analytic tools; G.S., N.K.S., L.W., I.B., X.C., M.B., E.-E.B., F.C., E.P., and C.M. analyzed data; and E.-E.B., E.P., and C.M. wrote the paper.

Reviewers: R.M.S., University Clinic Leipzig; and C.V.-G., University of British Columbia.

The authors declare no conflict of interest.

[1]G.S. and N.K.S. contributed equally to this work.

[2]To whom correspondence may be addressed. Email: etienne.baulieu@inserm.fr or Charbel.massaad@parisdescartes.fr.

This article contains supporting information online at www.pnas.org/lookup/suppl/doi:10.1073/pnas.1715999115/-/DCSupplemental.

They bind specific responsive elements called Xenobiotic responsive elements (XREs), located in the promoter regions of the target genes, consequently leading to their transactivation (e.g., Cytochrome 1A1). Nevertheless, its endogenous functions begin to emerge, and natural ligands of the AHR, like tryptophan derivatives, were identified. The AHR is present in ancient invertebrate organisms like *Caenorhabditis elegans*, where it is responsible for the regulation of GABAergic neuron fate specification (18). Kynurenine is a tryptophan catabolite generated via Tryptophan Dioxygenase (TDO) and Indoleamin 2,3-Dioxygenases (IDO). By activating AHR, kynurenine promotes tumor-cell survival and malignancy of glioma (19). Despite the discovery of the cognate ligand of AHR, the endogenous role of the AHR remains poorly explored, especially in the peripheral nervous system.

In this study, we report an up-regulation of AHR signaling in PNFs and MPNSTs. Furthermore, the inhibition of AHR promotes MPNST cell apoptosis. On the other hand, we investigate the role of AHR in normal SC physiology and myelin gene regulation using $Ahr^{-/-}$ mice. These mice have thinner myelin sheaths, dysregulated myelin gene expression, and consequent locomotor deficiencies. Taken together, our results elicit a role of the AHR in peripheral myelin gene regulation and a stimulation of AHR activity in malignant transformation of peripheral nerve sheath tumors. Our results also suggest that targeting AHR could be a promising avenue in the treatment of PNFs and MPNSTs.

Results

AHR Signaling Pathway Is Activated in Peripheral Nerve Sheath Tumorigenesis. In a series of 38 tumors, we first analyzed mRNA expression of *AHR*, *AHRR* (AHR Repressor), and *ARNT* (Table 1). *AHR* was significantly up-regulated in PNFs (sevenfold) and in MPNSTs (ninefold), compared with the dermal neurofibromas. *AHRR* was significantly down-regulated in PNFs (threefold) and MPNSTs (twofold) compared with the dermal neurofibromas, while *ARNT* expression was not significantly altered in either the PNFs or the MPNSTs.

Several genes implicated in the AHR pathway were also tested, including kynurenine metabolism (*IDO1*, *IDO2*, and *TDO2*), inflammation and immune pathways (*IL-1β*, *IL-6*, *IL-8*, *CXCL5*, and *CXCL6*), SC markers (*S100B* and *P0*), and proliferation (*MKI67*). *IDO1* and *TDO2* (but not *IDO2*) were significantly up-regulated in PNFs and MPNSTs. Concerning the inflammatory pathway, *IL-1β*, *IL-6*, *IL-8*, *CXCL5*, and *CXCL6* mRNA levels showed significant overexpression in PNFs and MPNSTs, compared with the dermal neurofibromas (Table 1). It is noteworthy that *AHR* and the enzymes of its endogenous ligands are remarkably higher in MPNSTs than in PNFs. The proliferation-associated gene *MKI67* was overexpressed in the MPNSTs. SC-specific gene (*S100B*, *P0*) expression was shown to be significantly down-regulated in MPNSTs.

We also performed an immunostaining of AHR in MPNSTs (Fig. 1). We detected strong nuclear AHR staining in a proportion of tumor cells, while intratumoral vessels and fibroblasts in a fibrous septum (taken as internal negative controls) were not stained. Altogether, our data show that the AHR pathway is activated in human PNFs and MPNSTs.

AHR Inhibition Induced Apoptosis in MPNST Cell Lines. As we observed, the AHR pathway is activated in human PNFs and MPNSTs. Subsequently, we hypothesized that inhibiting the AHR could affect MPNST cell survival. We used two AHR antagonists [CH-223191 (CH) and 6,2′,4′-trimethoxyflavone (TMF)] to inhibit AHR activity in STS26T. Treatment with CH (50 μM at 48 h and 72 h) modestly increased cell death and enhanced apoptosis and shifted to the late apoptotic state (double positive for both Annexin and PI cell population) as quantified by Annexin V and PI staining (Fig. 2*A*, 48 h, and Fig. 2*B*, 72 h and Fig. S1*A*). CH did not have any effect at 10 μM, whereas TMF exhibited a more potent effect on MPNST cell death even at 10 μM. TMF (10 μM, 48 h or 72 h) decreased cell viability by ∼50%. After incubation with TMF (10 μM, 72 h), ∼20% of the cells underwent apoptosis and 30% were late apoptotic. As expected, CH and TMF inhibited the expression of the AHR target gene *CYP1A1* (Fig. 2*C*). To confirm that this is due to AHR inhibition, we silenced *AHR* by *siAHR*. *AHR* silencing also induced apoptosis in STS26T dose-dependently (Fig. 2*D*). Silencing of *AHR* drastically decreased the mRNA levels of *AHR* and its target genes *CYP1A1* and *CYP1B1* (Fig. 2*E*). As the IL-1β expression was enhanced in PNFs and MPNSTs (Table 1), accordingly the inhibition of AHR either by siRNA or antagonists reduced *IL-1β* expression in STS26T cells (Fig. 2*F*).

We confirmed these results using another MPNST cell line, 90–8. As expected, CH inhibited the expression of the classical AHR target genes *CYP1A1* and *CYP1B1* (Fig. S2*A*). Treatment with CH (50 μM) increased the number of dead cells (Fig. S2 *B* and *C*) and enhanced apoptosis. We confirmed this result with *siAHR* (Fig. S2 *D* and *E*). Furthermore, it also reduced the expression of *IL-1β* (Fig. S2*G*).

***Ahr* Ablation in Mice Caused Locomotor Defects and Led to Thinner Myelin Sheath.** Given the fact that PNF and MPNST are complex tumors with different cells, we analyzed the expression of *AHR* and related components in different cells like SCs, mast cells, and endothelial cells. *AHR* mRNA is predominant in SCs and may suggest its importance in SC physiology (Table 2). The observed activation of the AHR pathway and the down-regulation of the myelin gene (*P0*) and as well as *S100B* in PNFs and MPNSTs compelled us to investigate further the role of AHR in normal SCs. Henceforth, we analyzed AHR expression in sciatic nerves and SCs (Fig. 3 *A*–*C*). AHR is expressed in the nerve (Fig. 3 *A* and *C*) and is localized in the nucleus of an SC as well as the perinuclear compartment (Fig. 3*B*).

We analyzed the locomotor behavior of $Ahr^{-/-}$. We measured stride time using a motorized treadmill (Fig. 3*D*). No significant difference was observed with treadmill speed at 10 cm/s. However, when the treadmill speed was increased at 16 cm/s, $Ahr^{-/-}$ mice showed a slower stride than WT mice. At a higher speed, $Ahr^{-/-}$ mice were not able to maintain the rhythm and therefore could not be tested.

Mice were then subjected to fixed speed rotarod protocol (14 rpm) for 5 consecutive days where the time to withstand the rotating rod was measured (Fig. 3*E*). The WT mice significantly improved their performance over days, indicating an amelioration of their motor coordination, whereas the time latency of $Ahr^{-/-}$ mice remained constant. Indeed, WT mice were able to stay on the rotating bar on day 5 for 207 ± 100 s, while $Ahr^{-/-}$ mice remained only for 12 ± 3 s. Our findings suggest that the $Ahr^{-/-}$ mice have impaired locomotion and motor coordination. Then, we performed the static rod test (Fig. 3*G*). All WT mice stayed 100 s on the bar. In contrast, $Ahr^{-/-}$ mice were unsuccessful in staying (Fig. 3*H*). Finally, motor performance was evaluated using a dynamic rod test. The $Ahr^{-/-}$ mice were three times slower than the WT mice in crossing the rod (Fig. 3*I*). The $Ahr^{-/-}$ mice also exhibited more faults while crossing the rod (Fig. 3*I*).

We studied myelin structure by electron microscopy. The myelin sheath of $Ahr^{-/-}$ mice was significantly thinner than controls (Fig. 3 *J* and *K*), and the axonal perimeter was higher in $Ahr^{-/-}$ mice compared with controls (Fig. 3*L*). We plotted the g ratios of sciatic nerve fibers as a function of their respective axonal perimeters (Fig. 3*M*). We observed reduction in myelin thickness for all axon calibers, but smaller axons were more affected.

Western blot (WB) showed a significant increase of P0 and PMP22 in $Ahr^{-/-}$ sciatic nerves (Fig. 3*N* and Fig. S5). Consistent with these results, the expression of the negative regulator of myelination, SOX2, was reduced by 40% in $Ahr^{-/-}$ mice (Fig. 3*N*), while the expression of active β-catenin was enhanced by twofold and total β-catenin was decreased by 40%. Therefore, the ratio of

Table 1. Median mRNA levels and ranges of 16 genes in dermal and PNFs and MPNSTs

Genes	Dermal neurofibromas, $n = 8$		PNFs, $n = 16$		MPNSTs, $n = 14$		P*
	Median	Range	Median	Range	Median	Range	
AHR pathway							
AHR	**1.00**	0.13–11.59	**6.84**	0.01–71.01	**8.98**	0.57–63.28	**$P < 0.05$**
AHRR	**1.00**	0.56–8.44	**0.39**	0.13–1.60	**0.49**	0.07–1.80	**$P < 0.01$**
ARNT	**1.00**	0.76–3.38	2.12	0.65–5.78	1.71	0.49–7.62	NS
Trp metabolism							
IDO1	**1.00**	0.04–10.75	**2.98**	0.11–41.54	**49.38**	1.59–681.64	**$P < 0.01$**
IDO2	**1.00**	0.21–6.74	0.60	0.07–5.06	0.65	0.01–18.21	NS
TDO2	**1.00**	0.05–101.38	**7.21**	0.25–77.62	**24.77**	0.86–2,931.70	**$P < 0.01$**
Myelin SCs							
S100B	**1.00**	0.64–1.73	**0.82**	0.10–4.49	**0.02**	0.01–2.54	**$P < 0.01$**
MPZ	**1.00**	0.10–1.79	**0.46**	0.10–2.54	**0.01**	0.01–2.24	**$P < 0.01$**
Inflammation							
IL-1B	**1.00**	0.26–4.09	**19.44**	0.01–809.67	**6.15**	2.66–644.12	**$P < 0.05$**
IL-6	**1.00**	0.50–1.95	**19.86**	0.18–247.60	**25.67**	3.06–32.04	**$P < 0.05$**
IL-8	**1.00**	0.07–3.15	**8.98**	0.01–648.32	**13.65**	0.19–269.89	**$P < 0.05$**
CXCL5	**1.00**	0.08–40.19	**32.42**	0.01–643.00	**185.53**	0.17–25,864.45	**$P < 0.01$**
CXCL6	**1.00**	0.01–5.66	**10.86**	2.28–1,642.39	**24.33**	4.60–862.02	**$P < 0.01$**
Xenobiotics metabolism							
CYP1A1	**1.00**	0.01–1.88	2.16	0.10–18.85	1.50	0.40–4.11	NS
CYP1B1	**1.00**	0.49–5.78	1.01	0.12–9.07	0.69	0.11–4.42	NS
Proliferation							
MKI67	**1.00**	0.30–2.82	**1.39**	0.88–4.77	**31.43**	13.6–82.9	**$P < 0.01$**

AHR pathway is dysregulated in nerve tumors. Total RNA was isolated from patients having dermal neurfibromas ($n = 8$), PNFs ($n = 16$), and MPNSTs ($n = 14$). qRT-PCR was performed using primers recognizing specifically the genes indicated. Table indicates median and range mRNA levels. mRNA levels were normalized such that the median value of the dermal neurofibromas was 1. Kruskal Wallis H test was used to compare MPNSTs vs. PNFs vs. dermal neurofibromas. NS, not significant. The bold values are statistically significant ($P < 0.05$). *Kruskal Wallis H test: MPNSTs vs. PNFs vs. dermal neurofibromas.

active β-catenin to total β-catenin is increased 3.5-fold in $Ahr^{-/-}$ mice, suggesting an activation of the Wnt/β-catenin pathway.

***Ahr* Is Involved in Myelination During Development.** To determine when these myelin abnormalities arose, we analyzed the expression pattern of AHR during the myelination process at P7, P21, and in 8-wk-old (8WO) mice and compared it to the expression of positive modulators of the myelination process: KROX20 and β-catenin. As depicted in Fig. 4*A*, AHR expression was at the highest level at P7 and then decreased at later time points to reach its lowest level in adult mice. KROX20 expression gradually increased during the myelination process to attain the highest level at P21 and, as expected, dropped in adult animals. Finally, β-catenin increased at P21, and then its expression was brought back to the same levels of P7 and at 8WO.

Taking account of this difference in AHR expression during development, we analyzed the structure of myelin sheaths from sciatic nerves of P7 mice (Fig. 4*B*). We observed a mild disorganization of myelin sheaths in $Ahr^{-/-}$ mice without affecting the g ratio (Fig. 4*C*). A moderate increase of the axonal perimeter was detected in $Ahr^{-/-}$ mice (Fig. 4*D*). Nevertheless, $Ahr^{-/-}$ mice displayed fewer myelinated axons (28.88 ± 1.18 for WT vs. 20.88 ± 1.23 for $Ahr^{-/-}$; Fig. 4*E*). P0 (−50%) and PMP22 (−60%) protein expression was decreased in 7-d-old $Ahr^{-/-}$ mice (Fig. 4*F*). To explore if myelin gene inhibition is due to a dysregulation in the expression of the major transcriptional regulators of SC myelination, we quantified the expression of SOX2, KROX20, total β-catenin, and active β-catenin. The knockout of *Ahr* did not affect the expression of SOX2. However, we observed a decreased KROX20 expression (−60%) that was confirmed by immunohistochemistry experiments. We observed a 25% reduction in the number of KROX20-positive cells in the sciatic nerves as suggested by DAPI (Fig. 4*G*). Furthermore, WB analyses showed that active β-catenin expression was diminished by 30% in $Ahr^{-/-}$ nerves (Fig. 4*F*). As the amount of total β-catenin was increased in $Ahr^{-/-}$ mice (+35%), we observed a decrease in the ratio of active β-catenin to total β-catenin, suggesting an impairment of the Wnt/β-catenin pathway at P7 when *Ahr* is knocked out. At P21, electron microscopy images revealed that myelin sheaths are affected by the deletion of *Ahr* (Fig. 4*H*). The g ratio was decreased, designating thicker myelin sheaths around the axons of $Ahr^{-/-}$ mice (Fig. 4*I*). The axonal perimeter was reduced (Fig. 4*J*) while the numbers of myelinated were not affected in $Ahr^{-/-}$ mice (Fig. 4*K*).

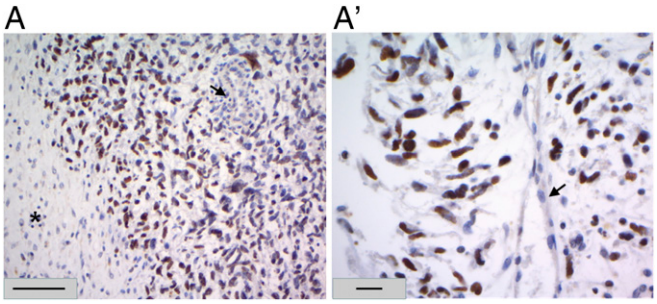

Fig. 1. (*A* and *A′*) AHR nuclear staining is detected in MPNST tissues. Formalin-fixed, paraffin-embedded human MPNST samples were stained with hematoxylin–eosin–saffron (HES), and AHR was revealed by a specific antibody. (*A*) A strong nuclear AHR staining was detected in a proportion of tumor cells, while intratumoral vessels (arrows) and fibroblasts in a fibrous septa (*) were not stained, taken as internal negative controls. (*A′*) A peroxidase technique, diaminobenzidine chromogen, and hematoxylin counterstain were employed. (Scale bar, 100 μm.)

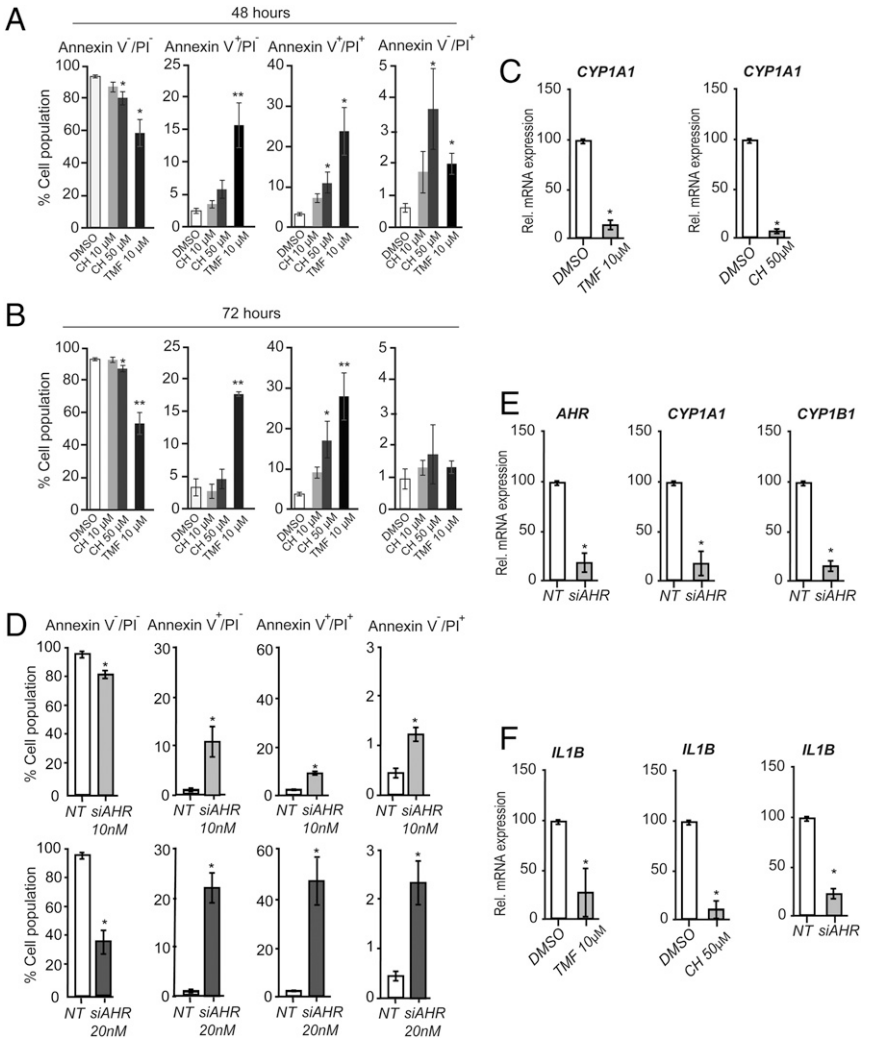

Fig. 2. AHR inhibition causes apoptosis in the MPNST cell line. (*A* and *B*) STS26T cells were treated with either AHR antagonists (CH or TMF) or DMSO (vehicle) for 48 h (*A*) or 72 h (*B*). Cells are stained with Annexin and PI to detect cell death by flow cytometry: living cell population (Annexin V^-/PI^-), apoptotic cells (Annexin V^+/PI^-), late apoptotic cells (Annexin V^+/PI^+), and dead cells (Annexin V^-/PI^+). Results represent the means ± SEM of at least four independent experiments. $*P < 0.05$, $**P < 0.01$, by Bonferroni's post hoc tests after one-way ANOVA compared with DMSO. (*C*) The STS26T cell line was treated with either AHR antagonists (CH or TMF) or DMSO (vehicle). Forty-eight hours later, total RNA was extracted and qRT-PCR was performed using primers recognizing *CYP1A1 and TBP* to normalize the results. They represent the means ± SEM of at least five independent experiments. $*P < 0.05$ by Student's *t* test compared with DMSO. (*D*) STS26T cells were transfected with either *siAHR* (10 nM and 20 nM) or *NT*; 72 h after medium change, cells were stained with Annexin and PI to detect cell death by flow cytometry: living cell population (Annexin V^-/PI^-), apoptotic cells (Annexin V^+/PI^-), late apoptotic cells (Annexin V^+/PI^+), and dead cells (Annexin V^-/PI^+). Results represent the means ± SEM of at least four independent experiments. $*P < 0.05$ by Bonferroni's post hoc tests after one-way ANOVA compared with control (*NT*). (*E*) STS26T cells were transfected with *siAHR* (20 nM) or *NT*; 72 h later, total RNA was extracted and qRT-PCR was performed using primers to amplify *AHR*, *CYP1A1*, and *CYP1B1*. Results were normalized to the *TBP* mRNA level and represent the means ± SEM of at least five independent experiments. $*P < 0.05$ by Student's *t* test compared with control (*NT*). (*F*) STS26T cells were reverse-transfected with *siAHR* (20 nM) or *NT* or incubated with CH (50 µM, 72 h), TMF (10 µM, 72 h), or DMSO. Total RNA was extracted and qRT-PCR experiments were performed using primers recognizing *IL-1β* and *TBP* to normalize. Results represent the means ± SEM of at least five independent experiments. $*P < 0.05$ by Student's *t* test compared with control (*NT*).

At P21, P0 and PMP22 expression were stimulated by twofold in $Ahr^{-/-}$ mice. SOX2 expression was still not affected, while the expression of all of the positive regulators was activated in $Ahr^{-/-}$ mice: KROX20 (+50%), total β-catenin (+60%), and active β-catenin (+35%) (Fig. 4*L*). Altogether, our data point out a crucial and differential role of *Ahr* during the myelination process and highlight that *Ahr* knockout leads to defects in myelin sheaths.

AHR Regulates Myelin Gene Expression in SCs. We transfected MSC80 cells with either nontargeting siRNA (*NT*) or *siAhr*. First, the efficacy of the knockdown was evaluated by qRT-PCR (Fig. S3*A*) and WB (Fig. S3*B*). In addition, we assessed the functional efficacy of the *siAhr* on *Cyp1A1*—luciferase activity that was reduced drastically (−80%) (Fig. S3*C*). The knockdown of *Ahr* increased mRNA levels of *P0* and *Pmp22* by 50% (Fig. 5*A*) and the promoter activity of *P0* and *Pmp22* (Fig. 5*B*). Taken together, the silencing of *Ahr* in the SC line or its knockout in mice led to a dysregulation of myelin gene expression.

Then, we examined the mechanism by which the AHR regulates myelin gene expression. We identified by MatInspector software four potential binding sites for AHR on the level of *P0* promoter and one putative AHR binding site on the *Pmp22* promoter (Fig. 5*C*). Therefore, we tested the AHR binding on *P0* and *Pmp22* promoters by ChIP. As a positive control, we assayed the binding of the AHR on the level of its target gene,

Table 2. Relative mRNA expression of eight genes in different human cells

Genes	SCs	Mast cells	Endothelial cell
AHR pathway			
AHR	426	11	6
AHRR	200	1,342	78
ARNT	1,105	492	479
Trp metabolism			
IDO1	10	NE	2
IDO2	NE	NE	NE
TDO2	14	3	NE
Myelin markers			
S100B	66,360	2	6
MPZ	24,336	4	5

AHR is predominantly expressed in SCs compared with mast cells and endothelial cells. Total RNA was isolated from normal human tissues. The gene mRNA levels (calculated as described in *Materials and Methods*) were based on the amount of the target message relative to the endogenous control *TBP* message, to normalize the starting amount and quality of total RNA. NE, not expressed.

Cyp1A1 promoter. As expected, the AHR bound to the *Cyp1A1* promoter (Fig. 5*D*). This binding was enhanced by twofold after treatment with TCDD (100 nM, 1 h). However, we did not detect AHR interaction with any of the putative binding sites identified on *Pmp22* (Fig. 5*E*) and *P0* (Fig. 5*F*), even after the incubation of MSC80 with TCDD (loading control, Fig. S4*A*). These data showed that AHR does not seem to interact directly with myelin gene promoters.

The other possible mechanism of action of AHR is the cross-talk with another signaling pathway. We previously showed that the activated Wnt/β-catenin pathway enhances the expression of peripheral myelin genes (12). Furthermore, we demonstrated that the knocking out of *Ahr* in mice altered β-catenin expression in the sciatic nerve (Fig. 3*N*). Therefore, we addressed the question of whether the action of AHR is mediated by the Wnt/β-catenin pathway. After silencing *Ahr* in MSC80 cells, we observed a 50% increase in the protein levels of active β-catenin and a 30% increase of total β-catenin levels (Fig. 5*G*). Furthermore, to support the hypothesis, knockdown of *Ahr* led to a significant stimulation of mRNA expression levels of Wnt signaling components *Lrp6*, *Dvl2*, *Dvl3*, and *Axin2* (Fig. 5*H*). Then, we assayed the functionality of the Wnt/β-catenin pathway. The SuperTOP Flash-Luciferase construct, bearing several binding sites for T cell factor/lymphoid enhancer factor (TCF/LEF), was activated by 2.5-fold 48 h after *siAHR* (Fig. 5*I*). To assess how AHR modifies β-catenin levels in MSC80 cells, we assumed that AHR is able to interact with β-catenin and stimulate its degradation as described in intestine cancer cells (20). Immunoprecipitation of AHR indicated protein–protein interaction of β-catenin and AHR in MSC80 cells (Fig. 5*J*).

Consequently, we hypothesized that the knockdown of *Ahr* increases the recruitment of β-catenin with TCF/LEF complex on the level of myelin gene promoters. We localized LEF/TCF–β-catenin binding sites on P0 and PMP22 promoters (12) (Fig. 5*K*). ChIP assays with β-catenin antibodies showed that *Ahr* silencing increased the recruitment of β-catenin on *P0* (Fig. 5*L* and Fig. S4*B*, loading control) and *Pmp22* promoters (Fig. 5*M* and Fig. S4*B*). Moreover, the binding of β-catenin was also enhanced after *Ahr* silencing on the level of a Wnt target gene, *Axin2* (Fig. S4*C*). GAPDH was used as a negative control (Fig. S4*D*). Collectively, these data demonstrate that AHR exerts its effect on myelin genes through the Wnt/β-catenin pathway.

Discussion

We reveal that AHR plays a crucial role in the myelination process of the nerve and is overexpressed in nerve tumors. We demonstrated that the AHR signaling pathway is activated in a series of NF1-associated nerve sheath tumors. We further analyzed other genes linked to the AHR and involved in tryptophan metabolism that lead to the synthesis of kynurenine, an endogenous ligand of AHR (20–22). The expression of two genes participating in the first steps of tryptophan metabolism, namely *IDO1* and *TDO2*, was significantly increased in PNFs and MPNSTs. *IDO1* and *TDO2* were found to be remarkably increased in malignant form compared with the benign form of these tumors, suggesting an increased AHR activity in the malignant transformation. The enzyme IDO1 mediates the first, rate-limiting, step in tryptophan metabolites to kynurenine and is up-regulated under an inflammatory microenvironment (23). Through generation of downstream metabolites, IDO1 enzyme activity may affect immunity, including specific immunomodulatory or cytotoxic functions (21). It has been reported that L-kynurenine activates AHR (19), which positively regulates IDO1 expression in immune cells, such as dendritic cells. Our observation showing a progressive up-regulation of *IDO1* and *TDO2* in PNFs (threefold and fivefold) and a further stimulation in MPNSTs (50-fold and 25-fold) suggests that kynurenine synthesis leading to AHR activation may play a role in peripheral nerve sheath tumor progression to malignancy.

In addition to the biallelic inactivation of the *NF1* gene, supplemental genetic lesions are necessary for malignant progression of PNFs. Alterations of additional genes (*CDKN2A/B*, *TP53*, *SUZ12*, *EED*) were detected in MPNSTs (3, 24). We have previously shown that the Wnt/β-catenin pathway was dysregulated in MPNSTs (15), and the present study reveals that the AHR pathway is also activated in these tumors. Furthermore, we have described an elevation of Wnt5a (15) and *AHR* expression in MPNST tumors. Conversely, the knockdown of *AHR* in MPNST cells inhibits Wnt5a expression (Fig. S2 *H* and *I*). Therefore, our data suggest a possible link between AHR and Wnt/β-catenin pathways in MPNSTs.

Consequently, we inhibited AHR in MPNST cell lines to alter their survival. Both AHR antagonists (CH or TMF) and *siAHR* induced apoptosis of two MPNST cell lines: 90–8 and STS26T. Again, this observation highlights the importance of AHR in SC malignancy in addition to *NF1*. Furthermore, AHR inhibition could down-regulate *IL-1β*, which was elevated in MPNST tumors. Previous results suggested that AHR activation coupled with inflammatory signals can lead to synergistic induction of IL-6 expression in tumor cells (25). We revealed a significant increase of *IL-1β*, *IL-6*, *IL-8*, *CXCL5*, and *CXCL6* mRNA levels in PNFs and MPNSTs. These results confirm previous in vitro findings showing that AHR activation may promote the induction of IL-6 and IL-8 (26, 27) and highlight the implication of AHR in the regulation of an inflammation pathway (28).

Previous studies from our laboratories and others have shown that some signaling pathways that are involved in the myelination process (Wnt/β-catenin, mTOR, ERK) are deregulated in MPNST (12, 29, 30). Therefore, we inquired about the endogenous role of AHR in normal SC physiology and peripheral nerve myelination. We revealed that AHR is expressed in SC and in the sciatic nerve and that $Ahr^{-/-}$ mice present an alteration in locomotion. Additionally, electron microscopy analyses depicted thinner myelin sheaths. These data unveil the role of AHR on SC myelinating functions. We performed electron microscopy analyses during the myelination process. They depicted a disorganization of myelin sheaths depending on the developmental stage. The first observation was that the myelin thickness was not affected at an early stage of myelination (P7). However, the number of myelinated axons was decreased in $Ahr^{-/-}$ mice, suggesting a delay in myelination. Then, we observed thicker myelin sheaths at P21, while adult animals had thinner myelin sheaths around the axons. These observations could be comparable to CMT1A patients (duplication of the *PMP22* gene) who

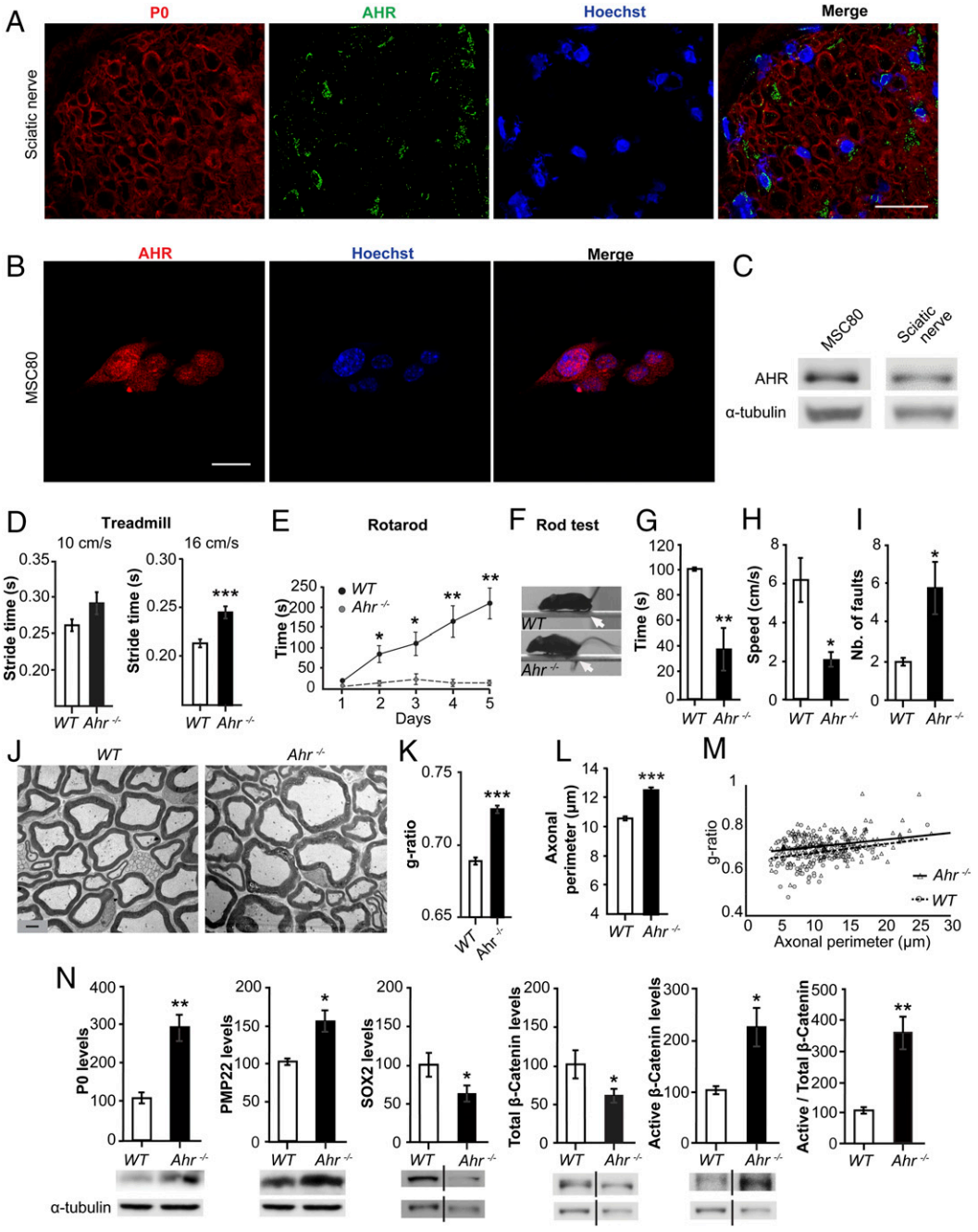

Fig. 3. *Ahr* ablation modifies myelin structure and locomotor behavior in adult mice. (*A*) Immunohistochemistry was performed on WT sciatic nerve to localize AHR (green) and P0 (red). The slides were imaged using a confocal microscope. This experiment was repeated at least three times, and a typical experiment is presented here. (Scale bar, 100 μm.) (*B*) An immunocytochemistry experiment was performed on MSC80 cells. AHR localization is highlighted in red; nuclei were stained with Hoechst (blue). This experiment was repeated at least three times, and a typical experiment is presented here. (Scale bar, 10 μm.) (*C*) WB showing the expression of AHR in MSC80 cells and in sciatic nerve. (*D*) In the gait parameter, 8-wk-old WT and $Ahr^{-/-}$ mice were placed on a treadmill at the speed of 10 cm/s and 16 cm/s. Stride time was measured, $***P < 0.001$ by Student's *t* test when $Ahr^{-/-}$ were compared with control mice. (*E*) For the rotarod test, 8-wk-old WT and $Ahr^{-/-}$ mice were subjected to the rotarod test for 5 d. The time that mice could stay on the rotarod was measured each day. At least five animals per group were tested. $*P < 0.05$, $**P < 0.01$ using Mann–Whitney test compared with control for each day of the experiment. (*F*) For the rod test, 8-wk-old WT and $Ahr^{-/-}$ mice were placed on the rod to perform either static or dynamic rod tests. Representative pictures of posture of the mice on the rod are shown. The arrowhead indicates right hind limb where the $Ahr^{-/-}$ mouse slipped (*G*) For the static rod test, measurement of the time that WT and $Ahr^{-/-}$ mice could stay without dropping from the rod. The test was stopped when mice succeeded in staying 100 s. (*H*) For the dynamic rod test, the average speed to cross the rod was measured (cm/s). (*I*) The number of faults (slips) counted for either WT or $Ahr^{-/-}$. At least five animals per group were tested. $*P < 0.05$, $**P < 0.01$ by Student's *t* test when $Ahr^{-/-}$ were compared with WT mice. (*J*) Sciatic nerves were isolated from either *WT* or $Ahr^{-/-}$ mice (8 wk old). Then, ultrathin (50–90 nm) cross-sections were prepared from Epon embedded nerves. (Scale bar, 2 μm.) (*K*) Myelin thickness was calculated by g-ratio determination. (*L*) Axonal perimeter was estimated using electronic microscopy pictures quantified by ImageJ software. At least five animals per genotype were used. (*M*) The g ratios were plotted against the axonal perimeter. (*N*) Adult male *WT* or $Ahr^{-/-}$ mice were killed, and then their sciatic nerves were dissected (at least $n = 6$ per group). Total proteins were extracted, and WBs were performed using antibodies against P0, PMP22, SOX2, KROX20, β-catenin, active β-catenin, and α-tubulin (loading control). Figures represent a typical experiment. WBs were quantified using ImageJ software. Black horizontal line between the lanes in the gels signifies a crop was made. Error bars indicate SEM. $*P < 0.05$, $**P < 0.01$ by Student's *t* test when $Ahr^{-/-}$ were compared with control mice.

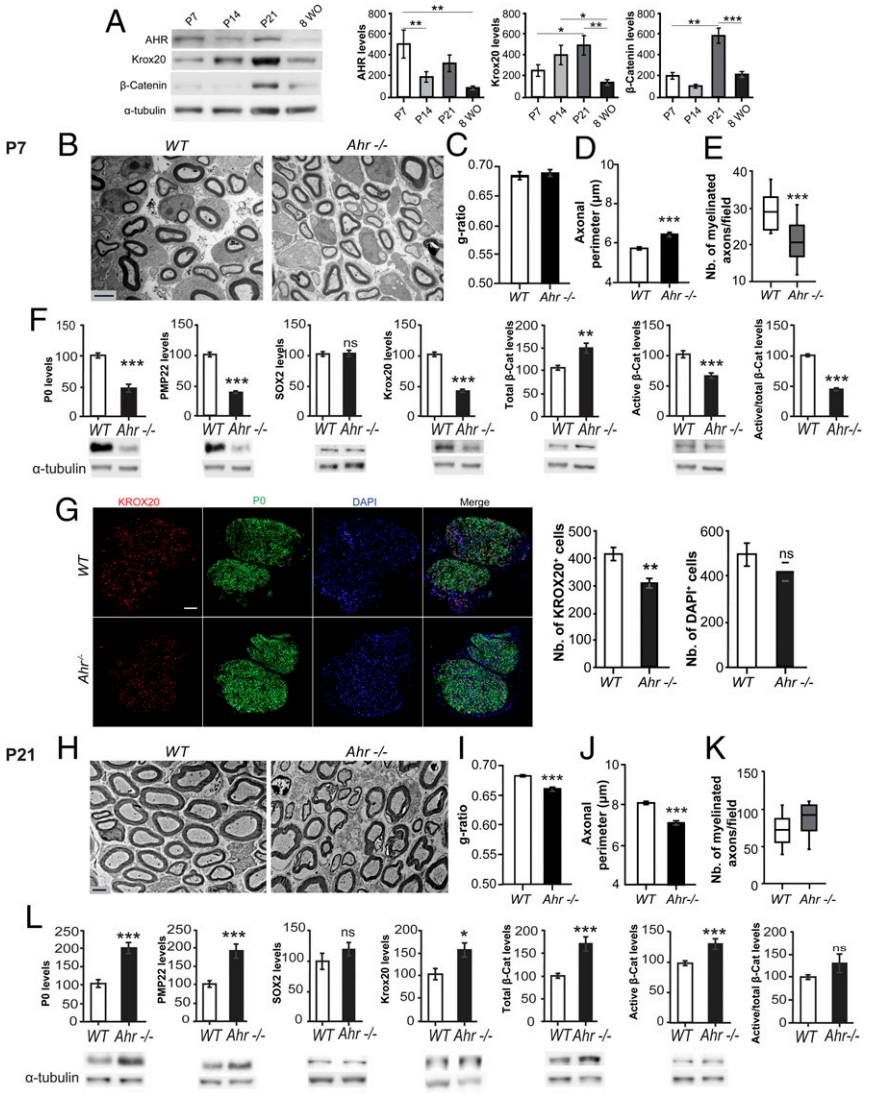

Fig. 4. The KO of *Ahr* alters myelin ultrastructure, myelin proteins, and myelination regulators during development. (*A*) Sciatic nerves from at least 4 mice of age P7 and P21 were extracted and total protein was prepared. AHR, KROX20, and β-catenin expression levels were determined by WB. α-tubulin served as the loading control. Figures represent a typical experiment. Ultrathin (50–90 nm) cross-sections were prepared from epon embedded P7, and P21 sciatic nerves. (*B*) Electron micrographs of P7 mice. (Scale bar, 2 μm.) (*C*) Myelin thickness of P7 mice sciatic nerves was estimated by g-ratio determination using electron microscopy pictures quantified by Image J software. (*D*) Axonal perimeter was measured by ImageJ software. (*E*) The number of myelinated axons were counted in a given unit area. (*F*) P7 male WT or $Ahr^{-/-}$ mice were killed, and then their sciatic nerves were dissected (at least $n = 6$ per group). Total proteins were extracted, and WBs were performed using antibodies against P0, PMP22, SOX2, KROX20, β-catenin, active β-catenin, and α-tubulin (loading control). Figures represent a typical experiment. (*G*) Immunohistochemistry was performed on WT or $Ahr^{-/-}$ sciatic nerves (P7). The slides were analyzed with a confocal microscope: KROX20 (red), P0 (green), and DAPI (blue). This experiment was performed with at least four animals per each group, and a typical experiment was presented here. (Scale bars, 50 μm.) The number of KROX20-positive cells and DAPI-positive cells was counted by means of ImageJ. (*H*) Electron micrographs of P21 mice. (Scale bar, 2 μm.) (*I*) The g-ratio determination using electron microscopy pictures quantified by ImageJ software. (*J*) Axonal perimeter was measured. (*K*) The number of myelinated axons were counted in a given unit area. Error bars indicate SEM. (*L*) P21 male WT or $Ahr^{-/-}$ mice were killed, and then their sciatic nerves were dissected (at least $n = 6$ per group). Total proteins were extracted, and WBs were performed using antibodies against P0, PMP22, SOX2, KROX20, β-catenin, active β-catenin, and α-tubulin. Figures represent a typical experiment. WBs were quantified using ImageJ. Error bars indicate SEM. $*P < 0.05$, $**P < 0.01$, $***P < 0.001$, by Student's *t* test when $Ahr^{-/-}$ were compared with WT mice.

are hypermyelinated in early childhood and then, 1 y after, a hypomyelination of some fibers is observed; it is caused by demyelination and remyelination cycles (31). The *Ahr* constitutive invalidation also modified the perimeters of the axons, showing a correlation between the formation of the myelin sheaths and axonal development. However, we cannot exclude that could also affect neuronal development directly. Prenatal exposure of TCDD in rats provoked a delay in oligodendrocyte differentiation and maturation (32). TCDD could also disrupt the functions of AHR to provoke neuropathies. In fact, rats intoxicated by TCDD showed severe defects in myelin structure of tibial and sciatic nerve and reduction in nerve conduction velocity (33, 34). Our results reinforce not only the endogenous role of AHR in a normal myelination process but also the mechanism by which it regulates myelination.

P0 and PMP22 myelin proteins are essential for an adequate structure of myelin sheath. Indeed, their dysregulation or mutation is deleterious for myelin sheath structure, leading to peripheral neuropathies. *P0* expression was drastically down-regulated in MPNST, and the knockout of *AHR* enhanced *P0* expression in SCs.

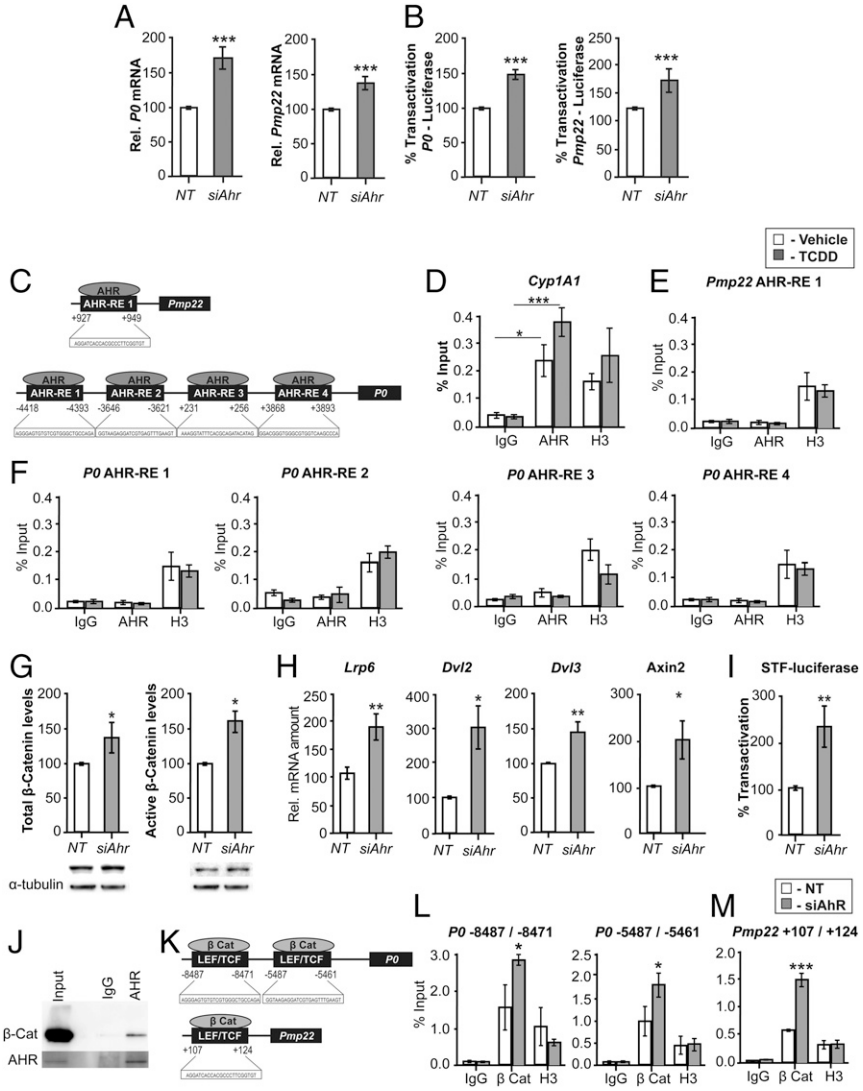

Fig. 5. AHR does not bind to myelin gene promoters in MSC80 cells but acts via the Wnt/β-catenin pathway. MSC80 cells were transfected with a siRNA directed against *Ahr* (*siAHR*) or a *NT* siRNA (*NT*). (*A*) Total mRNA was extracted, and *P0* and *Pmp22* transcripts were quantified by qRT-PCR. All results were normalized to the 26S mRNA level. (*B*) MSC80 cells were cotransfected with *siAhR* or *NT* and P0-luciferase or PMP22-luciferase constructs. Luciferase activity was assayed. Results represent the means ± SEM of at least five independent experiments. ***$P < 0.001$ by Student's *t* test compared with control (*NT*). (*C*) Putative binding sites of AHR located on the levels of P0 and PMP22 were identified by means of MatInspector software. MSC80 cells were incubated with vehicle (Nonane) or TCDD (100 μM, 24 h). ChIP assays with antibodies against AHR or Mock IgG (nonrelevant negative control) or Histone H3 (positive control) were performed. qRT-PCR was performed with primers recognizing AHR putative sites located on (*D*) *Cyp1A1*, an AHR target gene; (*E*) *Pmp22*; and (*F*) *P0* genes. Results represent the means ± SEM of at least four independent experiments. *$P < 0.05$ and ***$P < 0.001$ by Tukey's post hoc tests after one-way ANOVA compared with control. (*G*) MSC80 cells were transfected with siRNA directed against *Ahr* (*siAhr*) or a nontargeting siRNA (*NT*) for 48 h. Total proteins were extracted, and WBs were performed using antibodies against total β-catenin or active β-catenin and α-tubulin as a loading control. Figures represent a typical experiment. WB quantifications were done using ImageJ software. (*H*) Total RNA was extracted, and qRT-PCR experiments were performed using primers recognizing *Lrp6*, *Dvl2*, *Dvl3*, and *Axin2*. RT-PCR was normalized using 26S RNA. Data represent the mean ± SEM of at least four independent experiments. (*I*) MSC80 cells were transiently transfected with SuperTOP Flash-luciferase (STF-Luciferase) and with either *siAHR* or *NT*. Forty-eight hours later, luciferase activity was analyzed. Results represent the means ± SEM of at least six independent experiments performed in duplicate. *$P < 0.05$, **$P < 0.01$, by Student's *t* test. (*J*) Coimmunoprecipitation assays were performed on MSC80 cell extracts using AHR, blotted for β-catenin by WB, and IgG was used as a control. (*K*) The binding sites for TCF/LEF–β-catenin are localized on the promoter level for *P0* and *Pmp22* as described in ref. 12. MSC80 cells were transiently transfected with either *siAhr* or *NT* for 48 h after; ChIP assays with antibodies against β-catenin or Mock IgG or Histone H3 were peformed. Primers recognizing TCF/LEF–β-catenin binding sites on the levels of *P0* (*L*) and *Pmp22* (*M*) were used. Results represent the means ± SEM of at four independent experiments. *$P < 0.05$, ***$P < 0.001$ by Tukey's post hoc tests after one-way ANOVA compared with control.

The knockout of *Ahr* severely altered *P0* and *PMP22* expression during myelin development. At P7, when AHR expression is supposed to reach its maximal expression, we observed an inhibition of P0 and PMP22 expression, while starting from P21 until adulthood the KO of *Ahr* increased the expression of myelin genes. Thus, it appears that AHR differentially regulates P0 and PMP22 during development. The dysregulation of the myelin gene could be attributed to a modification of developmental markers that modulate P0 and PMP22 expression. For example, at P7, the positive regulators of myelin gene expression (KROX20 and β-catenin) are down-regulated. This undoubtedly provoked the inhibition of P0 and PMP22. At later time points (P21 and adult), myelin genes are activated consequently to the *Ahr* ablation. Concomitantly, KROX20 and β-catenin are overexpressed and SOX2 (negative effector) is inhibited.

We confirmed that the knockdown of *Ahr* activates the Wnt/β-catenin pathway in the SC line. The expression of the major components of the canonical Wnt pathway (i.e., *Lrp6*, *Dvl2*, β-catenin, and *Axin2*) and Wnt target promoter (Super-TOP Flash) are enhanced after *Ahr* silencing. How could AHR stimulate P0 and PMP22 promoter activities? The first hypothesis is that AHR binds directly on the level of putative XREs present on P0 and PMP22 promoter regions. Unexpectedly, none of these binding sites recruited AHR even in the presence of the AHR agonist dioxin. Therefore, we postulated that the action of AHR is possibly mediated by β-catenin because we observed an increase of β-catenin binding on TCF/LEF binding sites of *P0* and *Pmp22* promoters after *Ahr* knockdown.

AHR has a dual function in regulating gene expression as a ligand-activated transcription factor and as an E3 ubiquitin ligase. Kawajiri et al. (20) showed that AHR E3 ubiquitin activity has a role in the β-catenin degradation pathway that is independent of the adenomatous polyposis coli system in intestine. We assume that the inhibition of AHR may reduce the degradation of β-catenin, which is consistent with (*i*) the direct interaction that we have detected between AHR and β-catenin proteins and (*ii*) the β-catenin increase observed after *Ahr* knockdown.

In conclusion, our findings unraveled that AHR is involved in the myelination process. This pathway is overexpressed in nerve tumors, which could also serve, along with Wnt/β-catenin pathway, as new markers for this specific type of cancer. As the inhibition of AHR induced apoptosis of MPNST cells, we can propose that this approach is further translatable. For instance, using either nanoparticles or adeno-associated virus (35) to deliver *siAHR* to induce apoptosis of these malignant cells could be suggested in adjuvant to existing chemotherapy with reduced doses. This approach can reduce complications like chemotherapy-induced peripheral neuropathy. Hence, our results indicate that AHR could represent a novel and potential therapeutic target for this type of peripheral nerve sheath tumor that is poorly responsive to existing chemotherapeutics.

Materials and Methods

Animals. *Ahr* knockout mice were a gift from Alvaro Puga, Center for Environmental Genetics, University of Cincinnati, College of Medicine, Cincinnati. $Ahr^{-/-}$ mice and WT controls were maintained on a mixed strain background (C57BL/6j:RJ) and housed in a temperature-controlled room with a 12 h light/dark cycle. All experiments were performed on age-matched male mice. Adult animals were fed ad libitum with water and Global-diet 2016S from Harlan. All aspects of animal care were approved by the ethical committee for animal research of the University Paris Descartes (CEEA.34).

Treadmill Test: Forced Locomotion. Adult male $Ahr^{-/-}$ ($n = 5$) and control mice were acclimated to the testing room for 24 h before each test. The forced locomotion of the mice was investigated using a commercial motorized treadmill. The speed of the treadmill was controlled by a tachymeter. After the habituation session (speed, 6 cm/s), mice were tested at a speed of 10 cm/s and 16 cm/s the next day.

Rod Test: Static Paradigm. The same set of animals were subjected to both the treadmill test and rod test. The setup consisted of a rod 9.5 mm in diameter and 5 cm in length. After a period of habituation, animals were securely placed on the rod. The ability of the animal to remain on the rod without falling was investigated for a maximum period of 100 s.

Rod Test: Dynamic Paradigm. Dark platforms were setup at one end of the rod, where the mice were let for habituation for 10 min. Mice were primed to walk from a starting point along the bar (70 cm long, 9.5 mm diameter) fixed 30 cm above the bench. Once the mice had succeeded in reaching the final destination several times by the priming procedure, the test was recorded in three trials. We calculated the speed and the number of faults.

Rotarod Test: Forced Paradigm. Balance and motor coordination was tested using a motorized rotarod LE8200 apparatus (Bioseb). Adult mice were placed on a rotating treadmill drum (3 cm diameter), and the mice's latency to fall during the first 5 min of the trial was noted. The average time of the fall for each trial was measured. Fixed-speed rotarod has been performed at 14 rpm for 5 consecutive days for WT mice and $Ahr^{-/-}$ mice ($n = 5$).

Transmission Electron Microscopy. Electron microscopy was done using fixed sciatic nerves following the protocol described previously (14). Electron microscopy images were used for calculating the g ratio by ImageJ.

Patients and Samples. After clinical examination, the surgical removal of dermal neurofibromas was proposed in case of esthetical burden. Resection or removal of PNFs was described previously (ethical authorization IRB-Human CPP17/79, A0296746) (15).

Expression of Genes Involved in the AHR Signaling Pathway in Patients' Samples. QRT-PCR was carried out as described previously (15).

Immunohistochemistry.
Human samples. Immunohistochemistry of patient samples was carried out as described previously (15). Immunostaining of AHR (rabbit polyclonal antibody clone H211; Santa Cruz) was done at 3 μg/mL after heat antigen retrieval in pH 6.0 citrate buffer. In all samples, we checked for the absence of staining in intratumoral vessels and fibroblasts as for internal negative controls.
Mouse samples. Sciatic nerves were dissected and immersed in 4% paraformaldehyde and embedded with Tissue-Tek. Sections (10 μm) were cut using Cryostat. Primary anitbodies against P0 (Aves Laboratories Inc.), AHR (Enzo), and KROX20 (Thermo Fisher Scientific) were used. Then, the samples were incubated at room temperature for 1 h, 30 min with the appropriate secondary antibody (Alexa Fluor 488 donkey anti-mouse, Cy3-conjugated AffiniPure Donkey anti-Rabbit, and Cy3-conjugated Affinity Pure Donkey anti-Chicken). Nuclei were stained with Hoechst 33342 (Pierce Biotechnology). Sections were imaged using a confocal microscope (LSM510; Carl Zeiss).

Cell Culture. The mouse SC line (MSC80) was maintained in DMEM supplemented with 10% decomplemented FCS (HyClone-Perbio), 1% penicillin, 1% streptomycin (Gibco), and 1% Glutamine. All cultures were grown at 37 °C in a humidified atmosphere of 5% CO_2.

The MPNST-derived cell lines STS26T and 90–8 were maintained in advanced RPMI-1640 with 15% heat-inactivated FBS, 2.75‰ Bovine Pituitary Extract, 100 U/mL penicillin, and 100 μg/mL streptomycin (Invitrogen).

Plasmids and Chemicals. p1646 (Cyp1A1-luc) was graciously provided by A. Puga, Cincinnati, OH. siRNAs directed against *Ahr* were purchased from Qiagen. The *Ahr* was targeted by four siRNAs recognizing four different regions of the *Ahr* transcript. TCDD was purchased from LGC standards and CH-22319 and TMF from Sigma.

Transient Transfections. MSC80 cells (2.5×10^5 cells per well) were grown in six-well plates, transfected using Effecten reagents according to the manufacturer's instructions (Qiagen), and luciferase activity was determined using the enzymatic method described previously (36). The β-galactosidase activity was used to normalize the transfection efficiency.

STS26T or 90–8 cells were transfected with either *NT* siRNA (DHARMACON) or *siAHR* (DHARMACON) using RNAiMAX (Thermo Fisher Scientific) according to the manufacturer's instruction.

WB. WB assay was performed using the standard techniques. Primary antibodies against P0 and PMP22 were purchased from Abcam and Sigma, respectively; β-catenin from BD Transduction; active β-catenin from Millipore; α-tubulin from Sigma; SOX2 from Abcam; and AHR from Enzo Life Science (Biomol SA-210).

qPCR for MSC80. Total RNA from cultured MSC80 was extracted using TRIzol Reagent (Invitrogen) according to the manufacturer's instructions. qPCR was done as described previously (14). All results were normalized to the *26S* mRNA level and calculated using the ΔCt method. The primer sequences used in real-time qPCR are listed in Table S1.

ChIP. MSC80 cells (10^7) were fixed with 1% formaldehyde for 10 min. The cross-linking was quenched with 0.125 M glycine for 10 min. Fixed chromatin was then isolated and physically sheared by sonication to obtain DNA fragments 300–600 bp in length. Immunoprecipitation was done using Protein A/G magnetic nanobeads (Dynabeads Life Technologies). The antibodies used in ChIP assays were as follows: 5 μg of AHR-specific antibody (Biomol SA-210), 5 μg of β-catenin (BD Transduction #610154), Histone H3

(Cell Signaling 2650), and 5 μg Rabbit IgG (Sigma I5006). qRT-PCRs were done as mentioned earlier, with the primer pairs listed in Table S1. Then, the percentage of input was calculated as mentioned in ref. 37.

Co-Immunoprecipitation. MSC80 cell lysates were precleared with protein-A (Dynabeads Life Technologies), and then the total protein was measured with BioRad RCDC. The lysate was treated with DNase to digest the genomic DNA. We used 3 μg of AHR antibody (Biomol SA-210) to enrich AHR in 100 μg of total protein by using protein A Dynabeads (Rabbit IgG was used as the negative control). Finally, the enriched protein samples were blotted with usual standard WB techniques with β-catenin antibody (Biomol SA-210).

Flow Cytometry Analysis. STS26T or 90–8 cells cultured in 12-well plates were treated with AHR antagonists or DMSO. Cells undergoing apoptosis at the indicated time were identified using the Annexin V-FITC apoptosis detection kit (Abcam ab14085), following the manufacturer's instructions. BD FACS-CantoII was used. A total of 10,000 events were recorded at a light scatter to exclude debris and aggregated with a flow rate of less than 200 cells per second for each assay. The compensations and the settings were adjusted according to the assay. Data were analyzed using FlowJo Software.

Statistical Analysis. Unless otherwise specified, means of treatment groups were compared with one-way analysis of variance (ANOVA). When the ANOVA showed that there were significant differences between the groups, Tukey's test was used to identify the sources of these differences. $P \leq 0.05$ was considered statistically significant. Two group comparisons were performed by the Student's *t* test. As the mRNA levels did not fit a Gaussian distribution in human samples, (*i*) the mRNA levels in each subgroup of samples were expressed as their median values and ranges, rather than their mean values and coefficients of variation, and (*ii*) comparison between the three types of nerve sheath tumors was assessed by using the nonparametric Kruskal Wallis H test. Differences were considered significant at confidence levels greater than 95% ($P < 0.05$).

ACKNOWLEDGMENTS. The authors acknowledge Dr. Alain Schmitt of the Cochin Imaging Facility, Jean-Maurice Petit of the Imaging Facility des Saints Pères, and Stephanie Dupuy from the flow cytometry facility. This work was funded by INSERM, University Paris Descartes, the Agence National pour la Recherche (ANR), and the Agence Nationale de Sécurité Sanitaire de l'Alimentation, de l'Environnement et du travail (ANSES). G.S., N.K.S., M.H., and A.C. received PhD fellowships from the French Ministry of Research (MNRT). L.J. received a PhD fellowship from Region Ile de France.

1. Friedman JM (1999) Epidemiology of neurofibromatosis type 1. *Am J Med Genet* 89: 1–6.
2. Sabbagh A, et al.; Members of the NF France Network (2009) Unravelling the genetic basis of variable clinical expression in neurofibromatosis 1. *Hum Mol Genet* 18: 2768–2778.
3. Tucker T, Wolkenstein P, Revuz J, Zeller J, Friedman JM (2005) Association between benign and malignant peripheral nerve sheath tumors in NF1. *Neurology* 65:205–211.
4. Serra E, et al. (1997) Confirmation of a double-hit model for the NF1 gene in benign neurofibromas. *Am J Hum Genet* 61:512–519.
5. Cichowski K, Jacks T (2001) NF1 tumor suppressor gene function: Narrowing the GAP. *Cell* 104:593–604.
6. Chen Z, et al. (2014) Cells of origin in the embryonic nerve roots for NF1-associated plexiform neurofibroma. *Cancer Cell* 26:695–706.
7. Wu J, et al. (2008) Plexiform and dermal neurofibromas and pigmentation are caused by Nf1 loss in desert hedgehog-expressing cells. *Cancer Cell* 13:105–116.
8. Garbay B, Heape AM, Sargueil F, Cassagne C (2000) Myelin synthesis in the peripheral nervous system. *Prog Neurobiol* 61:267–304.
9. Nave K-A, Werner HB (2014) Myelination of the nervous system: Mechanisms and functions. *Annu Rev Cell Dev Biol* 30:503–533.
10. Niemann A, Berger P, Suter U (2006) Pathomechanisms of mutant proteins in Charcot-Marie-Tooth disease. *Neuromolecular Med* 8:217–242.
11. Topilko P, et al. (1994) Krox-20 controls myelination in the peripheral nervous system. *Nature* 371:796–799.
12. Tawk M, et al. (2011) Wnt/beta-catenin signaling is an essential and direct driver of myelin gene expression and myelinogenesis. *J Neurosci* 31:3729–3742.
13. Le N, et al. (2005) Analysis of congenital hypomyelinating Egr2Lo/Lo nerves identifies Sox2 as an inhibitor of Schwann cell differentiation and myelination. *Proc Natl Acad Sci USA* 102:2596–2601.
14. Makoukji J, et al. (2011) Interplay between LXR and Wnt/β-catenin signaling in the negative regulation of peripheral myelin genes by oxysterols. *J Neurosci* 31: 9620–9629.
15. Luscan A, et al. (2014) The activation of the WNT signaling pathway is a hallmark in neurofibromatosis type 1 tumorigenesis. *Clin Cancer Res* 20:358–371.
16. Watson AL, et al. (2013) Canonical Wnt/β-catenin signaling drives human Schwann cell transformation, progression, and tumor maintenance. *Cancer Discov* 3:674–689.
17. Long X, et al. (2015) MMP-12-mediated by SARM-TRIF signaling pathway contributes to IFN-γ-independent airway inflammation and AHR post RSV infection in nude mice. *Respir Res* 16:11.
18. Huang X, Powell-Coffman JA, Jin Y (2004) The AHR-1 aryl hydrocarbon receptor and its co-factor the AHA-1 aryl hydrocarbon receptor nuclear translocator specify GABAergic neuron cell fate in C. elegans. *Development* 131:819–828.
19. Opitz CA, et al. (2011) An endogenous tumour-promoting ligand of the human aryl hydrocarbon receptor. *Nature* 478:197–203.
20. Kawajiri K, et al. (2009) Aryl hydrocarbon receptor suppresses intestinal carcinogenesis in ApcMin/+ mice with natural ligands. *Proc Natl Acad Sci USA* 106:13481–13486.
21. Mezrich JD, et al. (2010) An interaction between kynurenine and the aryl hydrocarbon receptor can generate regulatory T cells. *J Immunol* 185:3190–3198.
22. Zhai L, et al. (2015) The role of IDO in brain tumor immunotherapy. *J Neurooncol* 123: 395–403.
23. Litzenburger UM, et al. (2014) Constitutive IDO expression in human cancer is sustained by an autocrine signaling loop involving IL-6, STAT3 and the AHR. *Oncotarget* 5:1038–1051.
24. Zhu Y, Ghosh P, Charnay P, Burns DK, Parada LF (2002) Neurofibromas in NF1: Schwann cell origin and role of tumor environment. *Science* 296:920–922.
25. DiNatale BC, Schroeder JC, Francey LJ, Kusnadi A, Perdew GH (2010) Mechanistic insights into the events that lead to synergistic induction of interleukin 6 transcription upon activation of the aryl hydrocarbon receptor and inflammatory signaling. *J Biol Chem* 285:24388–24397.
26. Kolasa E, Houlbert N, Balaguer P, Fardel O (2013) AhR- and NF-κB-dependent induction of interleukin-6 by co-exposure to the environmental contaminant benzanthracene and the cytokine tumor necrosis factor-α in human mammary MCF-7 cells. *Chem Biol Interact* 203:391–400.
27. Vogel CFA, et al. (2014) Cross-talk between aryl hydrocarbon receptor and the inflammatory response: A role for nuclear factor-κB. *J Biol Chem* 289:1866–1875.
28. Hollingshead BD, Beischlag TV, Dinatale BC, Ramadoss P, Perdew GH (2008) Inflammatory signaling and aryl hydrocarbon receptor mediate synergistic induction of interleukin 6 in MCF-7 cells. *Cancer Res* 68:3609–3617.
29. Kendall JJ, et al. (2016) CK2 blockade causes MPNST cell apoptosis and promotes degradation of β-catenin. *Oncotarget* 7:53191–53203.
30. Brundage ME, et al. (2014) MAF mediates crosstalk between Ras-MAPK and mTOR signaling in NF1. *Oncogene* 33:5626–5636.
31. Gabreëls-Festen A, Wetering RV (1999) Human nerve pathology caused by different mutational mechanisms of the PMP22 gene. *Ann N Y Acad Sci* 883:336–343.
32. Fernández M, et al. (2010) A single prenatal exposure to the endocrine disruptor 2,3,7,8-tetrachlorodibenzo-p-dioxin alters developmental myelination and remyelination potential in the rat brain. *J Neurochem* 115:897–909.
33. Grehl H, Grahmann F, Claus D, Neundörfer B (1993) Histologic evidence for a toxic polyneuropathy due to exposure to 2,3,7,8-tetrachlorodibenzo-p-dioxin (TCDD) in rats. *Acta Neurol Scand* 88:354–357.
34. Grahmann F, Claus D, Grehl H, Neundörfer B (1993) Electrophysiologic evidence for a toxic polyneuropathy in rats after exposure to 2,3,7,8-tetrachlorodibenzo-p-dioxin (TCDD). *J Neurol Sci* 115:71–75.
35. Ali HM, et al. (2014) Effects of silencing the *RET/PTC1* oncogene in papillary thyroid carcinoma by siRNA-squalene nanoparticles with and without fusogenic companion GALA-cholesterol. *Thyroid* 24:327–338.
36. Massaad C, Garlatti M, Wilson EM, Cadepond F, Barouki R (2000) A natural sequence consisting of overlapping glucocorticoid-responsive elements mediates glucocorticoid, but not androgen, regulation of gene expression. *Biochem J* 350:123–129.
37. Frank SR, Schroeder M, Fernandez P, Taubert S, Amati B (2001) Binding of c-Myc to chromatin mediates mitogen-induced acetylation of histone H4 and gene activation. *Genes Dev* 15:2069–2082.